Supporting Information

Hydride–enhanced plasma catalysis enables ultrahigh–rate ammonia synthesis at room temperature and atmospheric pressure

Shijian Luo, Hao Chen, Yuran Yang, Yang Song, Yongduo Liu, Daojun Long*, Siguo Chen*, and Zidong Wei

State Key Laboratory of Advanced Chemical Power Sources (SKL–ACPS), School of Chemistry and Chemical Engineering, Center of Advanced Electrochemical Energy (CAEE), Institute of Advanced Interdisciplinary Studies, Chongqing University, Chongqing, 401331, China.

Table of Contents:

1. Supplemental experiment sections

Structure and composition of the catalysts. The nanostructures of the catalysts were generated via a Thermo Fisher Scientific Talos F200S transmission electron microscope (200 kV). The catalysts were thoroughly mixed with ethanol, placed on copper grids covered in an amorphous carbon layer, and allowed to dry before being observed under transmission electron microscopy. The phase composition, crystallinity and crystalline plane of the catalysts were characterized by the XRD–6000 (Cu Kα radiation, 40 kV, 40 mA) instrument with a scanning range of 2θ=10°~90° and a scanning speed of 20° min^{-1} with a step size of 0.02626. All phase analyses of the catalysts were carried out via standard powder diffraction cards as a reference. The catalysts' hytrogen vacancy was analysed from the EPR200–Plus system and DPLS3000 positron annihilation lifetime spectroscopy (PALS). The time channel width of our PALS measuring system reaches 10.4 ps. In the PALS test, the catalysts were pressed into pellets (~1 mm in thickness and 10 mm in diameter) and then sealed in a vacuum bag in the glove box to keep out air exposure during transportation. Next, a 30 μCi 22Na positron source was quickly sandwiched between two identical plane–faced pellets once they were taken out from the vacuum bags. All measurements were carried out at room temperature. The lifetime spectra were best fitted to three lifetime components using the LTv9 program and the counts of every spectrum were 4.0×10^6.

Determination of NH_3 by online mass spectrometry (MS). For online MS analysis, the dielectric barrier discharge (DBD) reactor was packed with 1 g of catalyst on quartz wool. To monitor the fluctuations in reactants and products in the plasma–catalytic ammonia synthesis at different ratios of N_2 to H_2, a typical experiment using the Multiple Ion Detection (MID) mode in online mass spectrometry (Hiden Analytical HPR20 EGA) was set. The N_2/H_2 mixtures at volume ratios of 1:3, 2:3, 1:1, 3:2 and 3:1 were successively injected into the DBD reactor to initiate the 30 minutes plasma–catalytic reaction. The N_2/H_2 mixture was diluted with argon (Ar) carrier gas because of the limited inlet H_2 concentration allowed in mass spectrometer. The analysis of the outlet reactants and products from the plasma–catalytic ammonia synthesis was conducted via online mass spectrometry.

Ammonia products collection. 200 mL of 1 M HCl were applied at the gas outlet to collect the NH_3 product. After the 500–h continuous test, the HCl adsorption solution was treated with a rotary evaporator to collect the NH_4Cl powder.

Determination of NH_4^+ and ND_4^+ by ^1H nuclear magnetic resonance. For the ^1H NMR test of NH_4^+ and ND_4^+, 50 mL of maleate acid aqueous solution (0.1 mg mL^{-1}) and 50 mL of HCl (0.1 mol L^{-1}) were mixed to collect the ammonia products. Then, 500 μL of the mixed solution and 100 μL of DMSO–d_6 were transferred to an NMR tube and analyzed by a Bruker AVANCE III HD 600 MHz spectrometer equipped with a cryoprobe and precise water suppression (zgpr pulse sequence) for 64 scans under 25°C.

$^{15}N_2$ isotopic labeling experiment. Isotope labeling experiment was carried out using $^{15}N_2$ as a feed gas. 0.1 M HCl solution was used to collect the $^{15}NH_3$ product. Prior to the test, the H_2SO_4 solution was purged with Ar gas for 1 h in order to remove the remaining $^{14}N_2$ and other contaminants. The $^{15}N_2$ gas was fed continuously during the $^{15}NH_3$ production experiments. The $^{15}NH_3$ in the post–tested solution was identified by ^1H NMR spectroscopy.

Detection of gas–phase H and NNH radicals. 100 mL of 0.01 M PBS (pH = 7.2) solution was mixed with 1 mL of 5,5–dimethyl–1–pyrroline–N–oxide (DMPO) as the radical trapping reagent. During the plasma–catalytic experiments, a 1.7 MHz ultrasonic atomization device (MSK–USP–G–LD) was employed to atomize the radical trapping reagent and inject it into the DBD reactor. The H_2, N_2 and N_2/H_2 (2:3) was used as the carrier gas for ultrasonic atomization in different experiments, respectively. The flow rate of the carrier gases was 30 mL min^{-1}.

After the plasma–catalytic experiments, the radical trapping agent remaining in the reactor was collected and further identified by an EPR spectrometer (EPR200–Plus) operating in the X band frequency of 9.8525 GHz at 25 °C.

Breakthrough experiment. The breakthrough curve of N_2 and H_2 on the TiH_2 catalyst was tested with a multiconstituent adsorption breakthrough curve analyzer from BeiShiDe Instrument (BSD–MAB). In a typical breakthrough experiment, 1 g of TiH_2 powder was packed into a column capped at both ends with silica wool. A N_2/H_2 mixture with a volume ratio of 2:3 was used as the feed gas. Before the test, the TiH_2 catalyst was activated at 200 °C for 120 minutes by purging with helium.

Measurement of reaction order. The kinetic behavior of the plasma–catalytic NH_3 synthesis reaction was observed by analyzing the average reaction rate. The power–law expression for the NH_3 production rate (r_{NH3}) in the plasma–catalytic NH_3 synthesis can be described as follows:

$$-\frac{dP_{NH_3}}{dt} = r_{NH_3} = kP_{N_2}{}^{\alpha} \times P_{H_2}{}^{\beta}$$

$$\ln(r_{CO}) = \ln(k) + \alpha \ln\left(P_{N_2}\right) + \beta \ln(P_{H_2})$$

Here, k and P represent the backward reaction rate constant and the partial pressures of feed gas (N_2 and H_2), respectively.

To extract relevant kinetic information, the plasma–catalytic NH_3 synthesis reaction was performed on a corundum tube reactor fixed with 100 mg of catalyst (supported with 500 mg of quartz wool) under an input power of 40 W. When studying the reaction order α for N_2 (or β for H_2), the partial pressure of N_2 (or H_2) was set to be larger than a fixed partial pressure of H_2 (or N_2), and the partial pressure of N_2 (or H_2) supplied was changed and replaced with Ar to keep a constant total flow rate when keeping a constant H_2 (or N_2) fraction and pressure. It is known that Ar can increase the electron density and the number of reactive particles in the plasma; however, the impact of Ar may be minimized in this particular study due to the low partial pressures of the reactants. This assumption was also considered in the previous literature [1]. In order to avoid diffusion effects when measuring the reaction rate, one common heuristic is that low conversions of the limiting reactant lead to a negligible reactant concentration gradient between the inlet and outlet, so that the reactor can be considered to operate at differential conversion with negligible effects from gradients in concentration. The low conversions were achieved by operating at sufficiently high ratios of the feed flow rate to the mass of the catalyst bed [2]. Therefore, the total flow rate of (Ar + N_2)/H_2 in a ratio of 2:1 was kept at 300 mL min^{-1} when P_{N2} was changed, while the total flow rate of N_2/(Ar + H_2) with a ratio of 1:5 was kept at 300 mL min^{-1} when P_{H2} was varied.

2. Characterization of the LiH, CaH_2 and TiH_2 catalysts

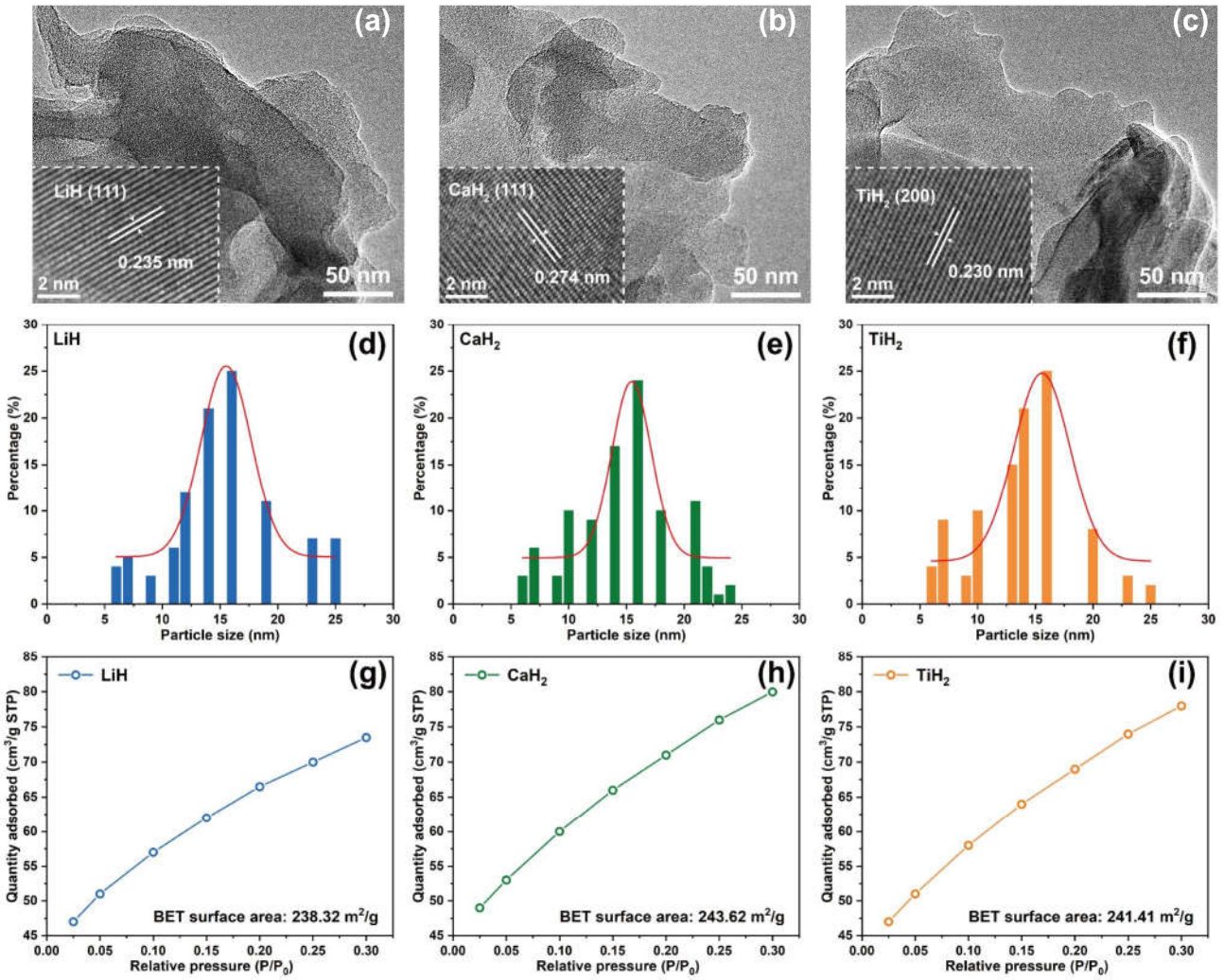

Figure S1 Transmission electron microscopy (TEM) images of (a) LiH, (b) CaH_2 and (c) TiH_2. Insets of (a−c) are the corresponding high–resolution TEM (HR–TEM) images for LiH, CaH_2 and TiH_2. Particle size distribution images of (d) LiH, (e) CaH_2 and (f) TiH_2. Brunner−Emmet−Teller (BET) measurements of (g) LiH, (h) CaH_2 and (i) TiH_2.

3. Plasma–catalytic test

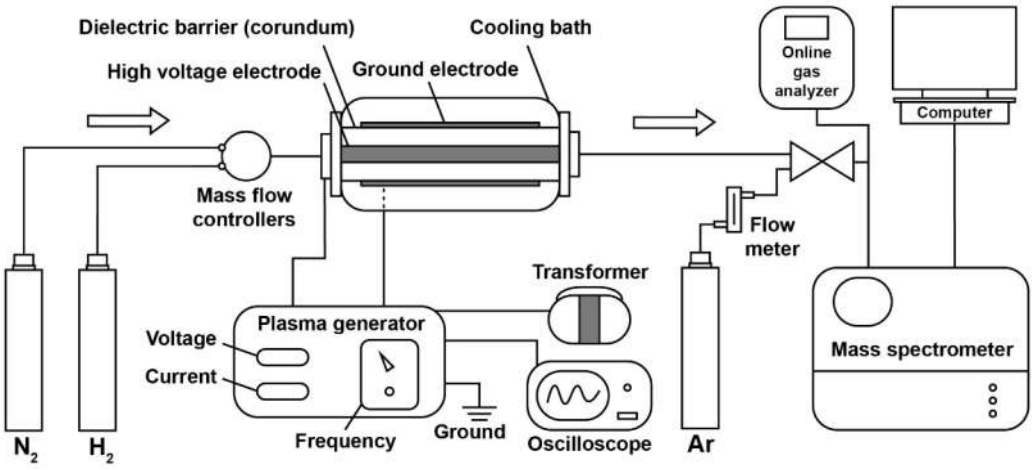

Figure S2 The schematic diagram of the plasma–catalytic ammonia synthesis reaction system.

The plasma–catalytic ammonia synthesis reaction over the catalysts was performed in a DBD reactor (Figure S2). The coaxial DBD reactor consisted of a corundum tube (20 mm i.d. × 25 mm o.d.) as the medium, a stainless steel rod (14 mm o.d.) coaxially positioned along the axis of the corundum tube as the high–voltage electrode to keep a 3 mm gas gap for the generation of plasma, and a stainless steel mesh wrapped outside the corundum tube as the ground electrode. A CTP–2000K high–voltage power source was applied to the DBD reactor (purchased from Nanjing Suman Plasma Technology). To ascertain the total charge (QT) or the discharge current (IT) transferred during the plasma reaction, measurements were taken on an external capacitor (C_{ext} = 47 pF) or an external resistor (R_{ext} = 50 Ω) connected to the ground electrode. All electrical signals were extracted from a Tektronix TBS1102 digital oscilloscope, operating at a 12–bit resolution and a sampling rate of 1 GS s^{-1}. To test the performance of the plasma–catalytic ammonia synthesis over the catalysts, 1 g of catalyst was distributed on quartz wool and then placed into the discharge area with a length of 150 mm and a gap of 3 mm (the area was between the corundum tube and the stainless steel high–voltage electrode). All hydride catalysts were pretreated using plasma cleaning equipment to remove any potential oxide layers from their surfaces prior to the performance tests. The N_2 and H_2 feeds were introduced by mass flow controllers (Hefei Kejing Materials Technology Co., Ltd., GSL–3Z). An online mass spectrometry (MS, Hiden HPR–20 EGA) was applied at the gas outlet for the qualitative analysis of the reactants and products. The reaction temperature of the system was maintain at 25 °C through the cooling bath. The catalyst performance was evaluated based on NH_3 synthesis rate (R_{NH_3}) and energy efficiency.

The NH_3 synthesis rate (R_{NH_3}) is calculated as the ratio of moles of ammonia to the amount of catalyst used in the performance tests. To make the performance more comparable, the amount of catalyst under "no catalyst" condition is assumed to be 1 g, which is the same amount as the catalysts used in other tests:

$$R_{NH_3}\ (mg/h/g) = \frac{Number\ of\ moles\ of\ produced\ ammonia\ (mg/h)}{The\ amount\ of\ catalyst\ used\ (g)}$$

The energy efficiency was determined by means of the following equation:

$$Energy\ efficiency\ (g{\cdot}kWh^{-1}) = \frac{C_{NH_3} \times Q_{gas-after}}{P_{Input}}$$

where C_{NH_3} is the concentration of ammonia generated in the plasma process, $Q_{gas-after}$ is the volumetric gas

flow rate after the reaction, and P_{Input} is the input power of the DBD plasma reactor.

The equations below are the definitions of specific energy input (SEI), which is defined as the input power divided by the gas flow rate:

$$SEI\ \ (kJ\ L^{-1}) = \frac{Power\ \ (kW)}{Flow\ rate\ \ (L\ min^{-1})} * 60\ \ (s\ min^{-1})$$

The output power was then calculated utilizing the Q–U Lissajous method, the equations below are the definitions of the discharge parameters:

$$S_{\text{Lissajous}} = \begin{matrix} i & j & k \\ x2-x1 & y2-y1 & 0 \\ x4-x1 & y4-y1 & 0 \end{matrix}$$

$$C_t = \frac{(y4-y3) * ky * C}{(x4-x3) * kx * k}$$

$$C_d = \frac{(y4-y1) * ky * C}{(x4-x1) * kx * k}$$

$$C_g = \frac{C_d * C_t}{C_d - C_t}$$

$$V_d = \frac{k * kx(x5-x6)}{2}$$

$$P_{out}\ \ (\text{W}) = \text{f} \times \text{k} \times \text{kx} \times \text{ky} \times S_{\text{Lissajous}}$$

where $S_{\text{Lissajous}}$ represents the area of Lissajou's plot (P1(x1, y1), P2(x2, y2), P3(x3, y3), P4(x4, y4)), C_t, C_d, C_g and V_d represent the cell capacitance, dielectric capacitance, discharge gap capacitance and breakdown voltage, respectively. P_{out}, f and C represent the discharge power, discharge frequency, sampling capacitance of the cell, respectively. The k, kx and ky voltage represent the sampling ratio, attenuation multiple of signal acquisition forthe CH1 channel and attenuation multiple of signal acquisition forthe CH2 channel, respectively.

The average electric field (E) is calculated from the parameters of Lissajous figures referred to the equation:

$$E = \frac{V_d}{d}$$

where d represents the discharge gap distance.

The reduced electric field (E/N) were calculated referred to the equation:

$$E/N = \frac{E}{P/\kappa_B T}$$

where E, P, K_B and T represent the average electric field, gas pressure, Boltzmann constant and gas temperature, respectively.

The Maxwellian EEDF in $eV^{-3/2}$ for mean electron energies from 0–70 eV in the plasma–only and plasma–catalytic systems using the open–access Boltzmann solver BOLSIG+.

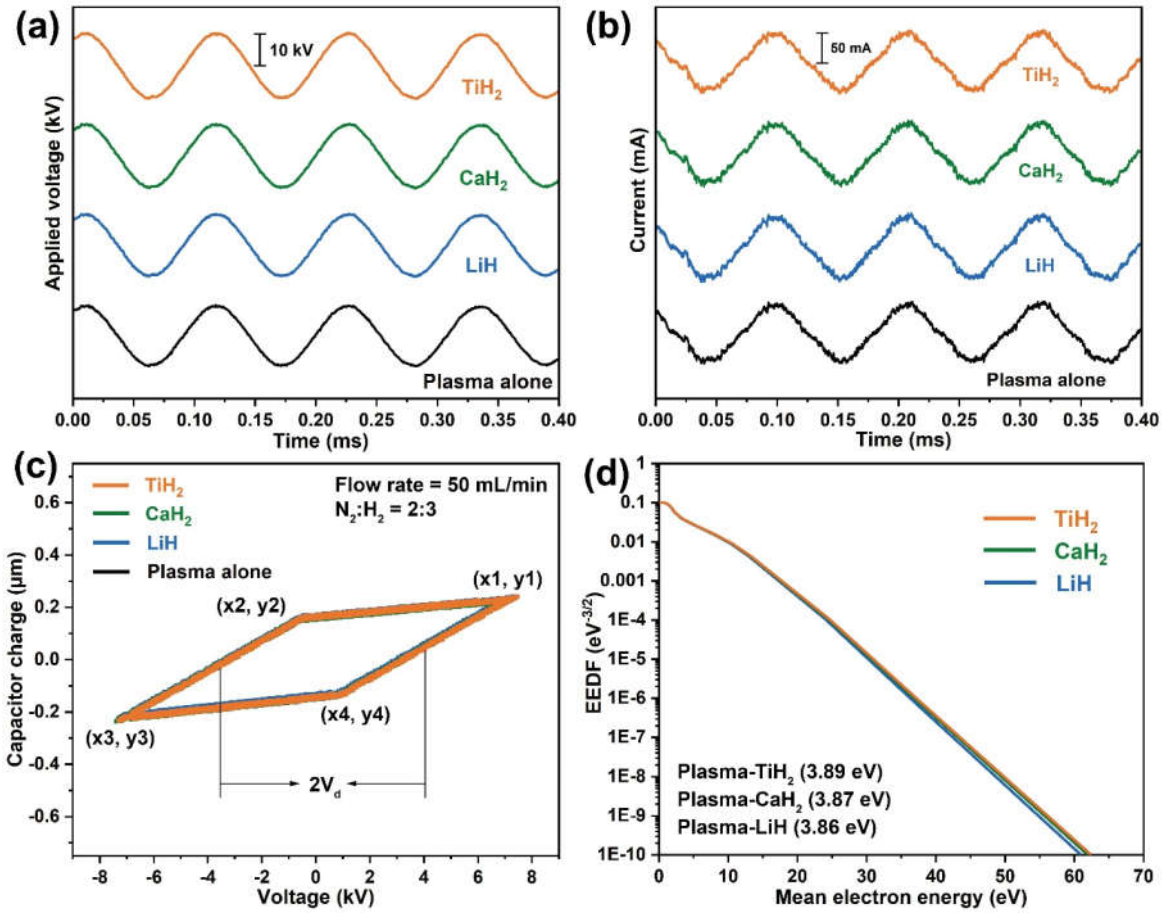

Figure S3 (a) Applied voltage signals, (b) current signals, (c) Lissajous plots and (d) Maxwellian EEDF in $eV^{-3/2}$ for mean electron energies from 0–70 eV in the plasma alone and plasma–catalytic systems (conditions: gas flow rate: 50 mL/min; N_2:H_2 = 2:3, catalyst loading: 1 g, input power: 40 W, discharge power: 32 W).

Table S1. Discharge parameters of the plasma alone and plasma–catalytic systems under N_2/H_2 (2:3) conditions.

	N_2:H_2 = 2:3							
	U_{pp} (kV)	C_t (μF)	C_d (μF)	V_d (kV)	f (kHz)	P_{out} (W)	E (kV/cm)	E/N (Td)
plasma–TiH_2	19.8	4.7	32.7	3.30	8.7	32.2	11.02	44.8
plasma–CaH_2	19.7	4.6	32.2	3.29	8.7	31.8	10.97	44.7
plasma–LiH	19.6	4.8	32.5	3.29	8.7	31.9	10.97	44.7
Plasma alone	19.2	4.9	33.9	3.28	8.7	31.3	10.93	44.4

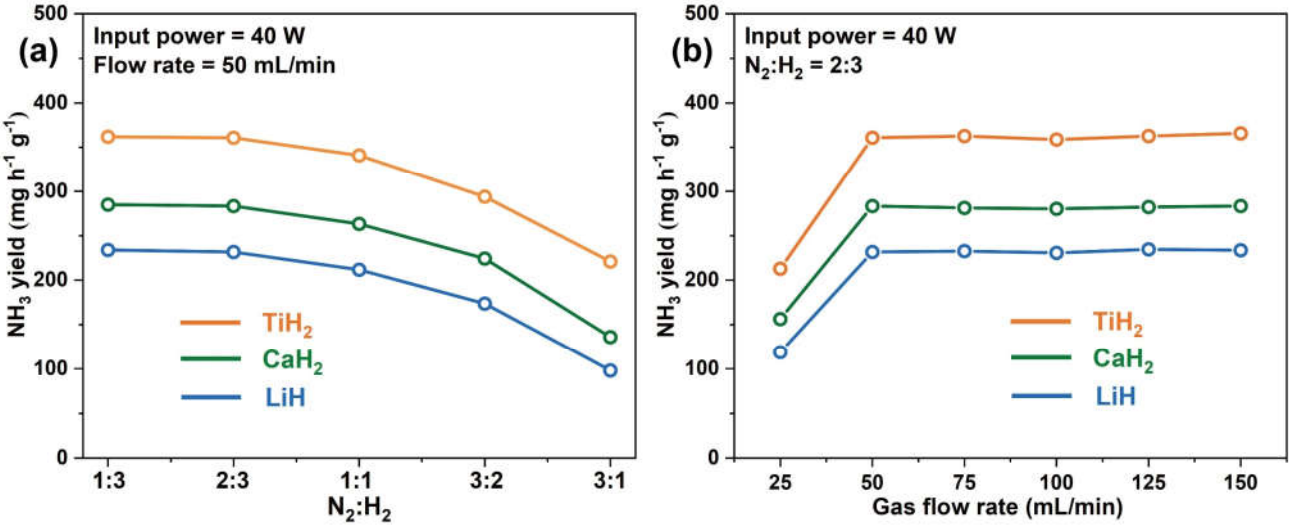

Figure S4 (a) NH_3 yields at different ratios of N_2 and H_2 over the LiH, CaH_2 and TiH_2 catalyst. (b) NH_3 yields at different gas flow rates over the LiH, CaH_2 and TiH_2 catalyst.

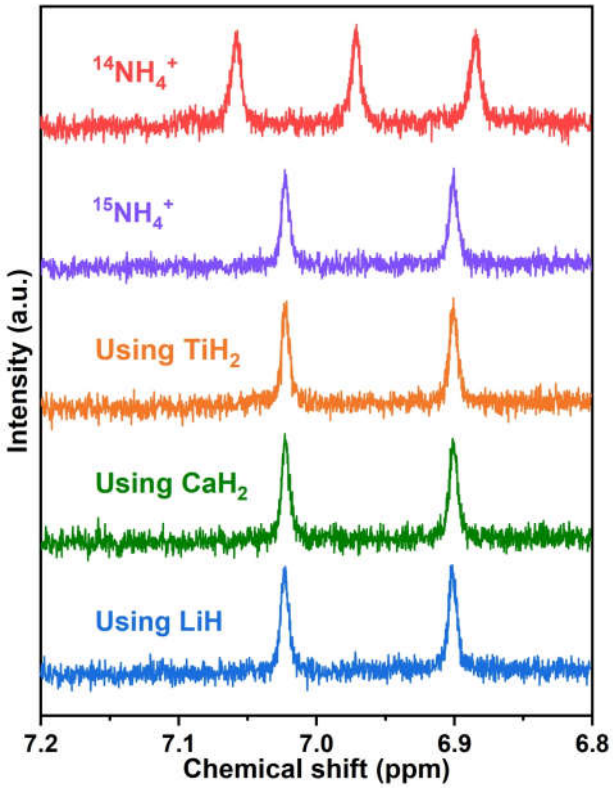

Figure S5 ^{1}H NMR spectra for $^{14}NH_4^+$ and $^{15}NH_4^+$ standard samples, and ^{1}H NMR spectra of ammonia absorption solution after reaction using $^{14}N_2$ and $^{15}N_2$ as the feeding gas.

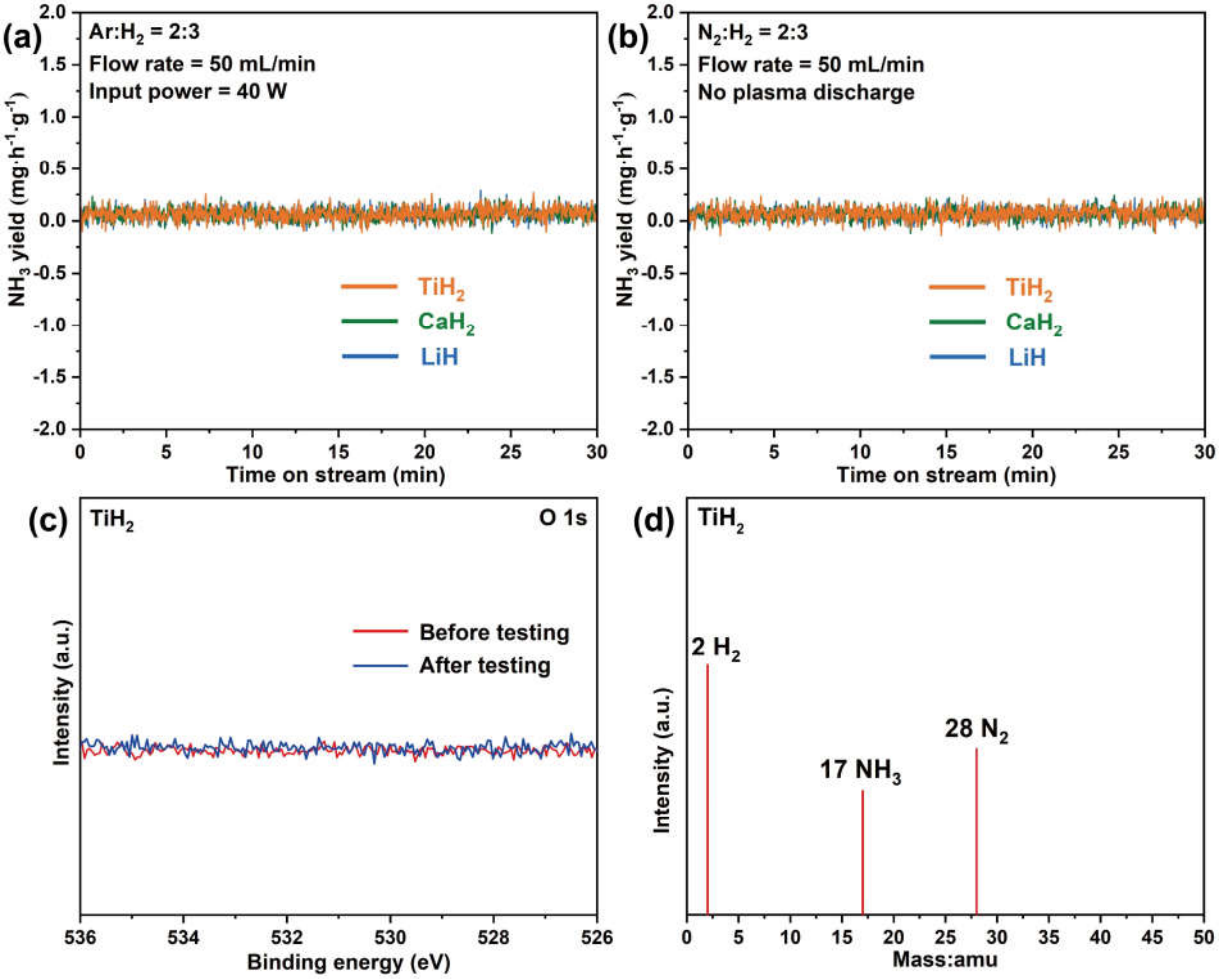

Figure S6 (a) 30 h plasma–catalytic NH_3 synthesis tests over the LiH, CaH_2 and TiH_2 catalyst under Ar/H_2 plasma condition. (b) The performance of ammonia synthesis without plasma discharge over the LiH, CaH_2 and TiH_2 catalyst. (c) O 1s XPS spectra of TiH_2 before and after the performance test. (d) Mass spectrometry analysis of outlet gas from the DBD reactor.

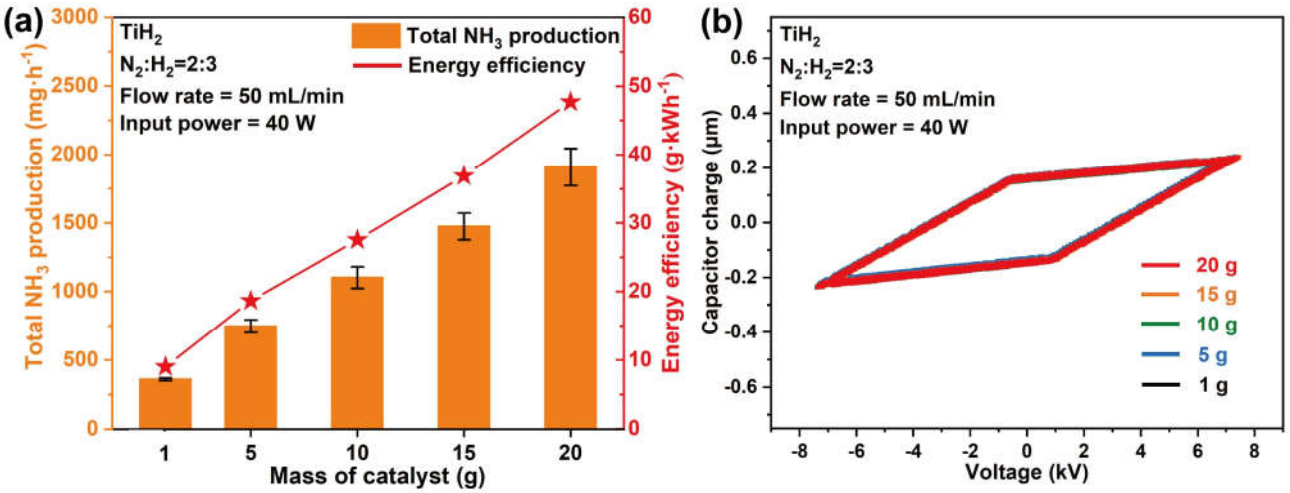

Figure S7 (a) Total NH_3 production and energy efficiency with different catalyst loadings of the TiH_2 catalyst. (b) Lissajous plots for the plasma–catalytic systems with different catalyst loadings of the TiH_2 catalyst.

4. Comparison of this work with other researches on ammonia synthesis

Table S2 Comparison of the current state–of–the–art performance in the plasma–catalytic ammonia synthesis using DBD plasma under mild conditions.

Catalyst	Loading mass (g)	Reaction Temperature (℃)	Reaction Pressure (Mpa)	N_2/H_2 ratios	NH_3 yield ($mg \cdot h^{-1} \cdot g^{-1}$)	Energy Efficiency ($g_{NH3} \cdot kWh^{-1}$)	Energy Consumption ($MJ \cdot mol^{-1}{}_{NH3}$)	Reference
TiH_2	1	25	0.1	2:3	360.9	9.02	6.78	This work
TiH_2	20	25	0.1	2:3	95.4	47.71	1.28	This work
CaH_2	1	25	0.1	2:3	283.3	7.08	8.64	This work
LiH	1	25	0.1	2:3	231.7	5.79	10.57	This work
OVs–CeO_2/CuO	1	200	0.1	2:3	196.2	1.96	31.22	[3]
VN	1	100	0.1	2:3	143.2	1.43	42.80	[4]
OVs–NVs–TiN/TiO_2	1	100	0.1	2:3	226.3	2.26	27.08	[5]
Ni/MCM	0.2	35	0.1	1:3	68.0	1.2	51.0	[6]
Ru/Al_2O_3	/	/	0.1	1:3	16.32	0.4	153.0	[7]
Ni/SiO_2	20	150	0.5	1:3	32.24	0.44	139.09	[8]
$BaTiO_3$	20	150	0.5	1:3	20.76	0.43	142.33	[8]
Ni/SiO_2–$BaTiO_3$	20	150	0.5	1:3	34.97	0.57	107.37	[8]
Ni/Al_2O_3	0.1	100	0.1	1:2	4.55	0.89	68.76	[9]

Ru/MgO	0.5	260	0.1	2:1	36.73	1.29	47.44	[10]
Zeolite–5A	0.1	120	0.1	1:3	15.81	0.513	119.30	[11]
$5Ru/Al_2O_3$	3.6	100	0.1	2:1	81.42	1.88	32.55	[12]
SBA–15	0.1	151	0.1	1:3	6.97	4.6	13.30	[13]
Ru/Carbon	0.2	/	0.1	1:3	5.46	0.72	85.0	[14]

Table S3 Comparison of the reported ammonia synthesis using electrocatalytic NRR (eNRR) at ambient conditions.

Cathode	Anode	Electrolyte	Feed gas	FE (%)	NH_3 yield ($mg \cdot h^{-1}$)	Energy Efficiency ($g_{NH3} \cdot kWh^{-1}$)	Energy Consumption ($MJ \cdot mol^{-1}_{NH3}$)	Reference
$Ru/2H–MoS_2$	Pt	0.01 M HCl	N_2	12.2	$2.64*10^{-3}$	33.42	29.92	[15]
Au/TiO_2	Pt plate	0.1 M HCl	N_2	8.1	0.021	114.94	8.70	[16]
$\gamma–Fe_2O_3$	IrO_2	0.1 M KOH	N_2	0.044	$9.8*10^{-4}$	136.99	7.30	[17]
Black phosphorus	Pt	0.01 M HCl	N_2	3.1	$6.3*10^{-3}$	31.25	32.00	[18]
THH Au NRs	Graphite	0.1 M KOH	N_2	4	$1.65*10^{-3}$	5.49	182.15	[19]
W_2N_3	Graphite	0.1 M KOH	N_2	11.7	$2.33*10^{-3}$	58.14	17.20	[20]
Pd/C	Pt mesh	0.1 M PBS	N_2	8.2	$1.35*10^{-3}$	27.03	36.99	[21]
$Au–CeO_x–rGO$	Pt	0.1 M HCl	N_2	10.1	$8.3*10^{-3}$	181.82	5.49	[22]

Table S4 Comparison of the reported ammonia synthesis using Li–mediated electrocatalytic NRR (Li–NRR) at ambient conditions.

Cathode	Anode	Electrolyte	Feed gas	FE (%)	NH_3 yield ($mg \cdot h^{-1}$)	Energy Efficiency ($g_{NH3} \cdot kWh^{-1}$)	Energy Consumption ($MJ \cdot mol^{-1}_{NH3}$)	Reference
Stainless steel cloth, GDE	Pt/SSC	1 M $LiBF_4$, 0.1 M EtOH	N_2	35	0.8	4.93	202.8	[23]
Stainless steel cloth, GDE	Pt/SSC	1 M $LiBF_4$, 0.1 M EtOH	N_2	35	0.8	2.40	416.7	[23]
Ag–Au@ ZIF	Pt wire	0.2 M $LiCF_3SO_3$, ~1% EtOH, THF	N_2	18	$2.89*10^{-5}$	13.44	74.4	[24]
Stainless steel cloth, flooded	Pt	$[C_4mpyr][eFAP]$	N_2	30	$1.4*10^{-3}$	87.49	11.43	[25]
Mo foil	Pt mesh	0.2 M $LiClO_4$, 0.18 M EtOH, THF	N_2	7.5	0.013	0.58	1731	[26]
polyimide/C	Pt	0.5 M Li_2SO_4/H^+	N_2	2.91	$4.7*10^{-4}$	6.09	164	[27]

Table S5 Comparison of the reported ammonia synthesis using the two–step integration of plasma N_2 oxidation (pNOR) with electrocatalytic reduction (eNO_xRR) at ambient conditions.

Catalyst for eNO_xRR	Electrolyte	FE (%)	NH_3 yield ($mg \cdot h^{-1}$)	Energy Efficiency ($g_{NH3} \cdot kWh^{-1}$)	Energy Consumption ($MJ \cdot mol^{-1}_{NH3}$)	Reference
$Ni(OH)_x/Cu$	1 M KOH	92	50.98	3.33	18.36	[28]
N–MoS_2/VGs	0.1 M KOH	97.6	7.3	25.5	2.4	[29]
Cu nanowires	0.01 M H_2SO_4	~100%	23.2	33.33	30.0	[30]
Ni_5P_4	1 M KOH	97.6%	9.52	6.83	8.96	[31]
$Pt/BaO/Al_2O_3$	/	/	30	29.14	2.1	[32]

5. Characterization of the LiH, CaH_2 and TiH_2 catalysts before and after the reaction

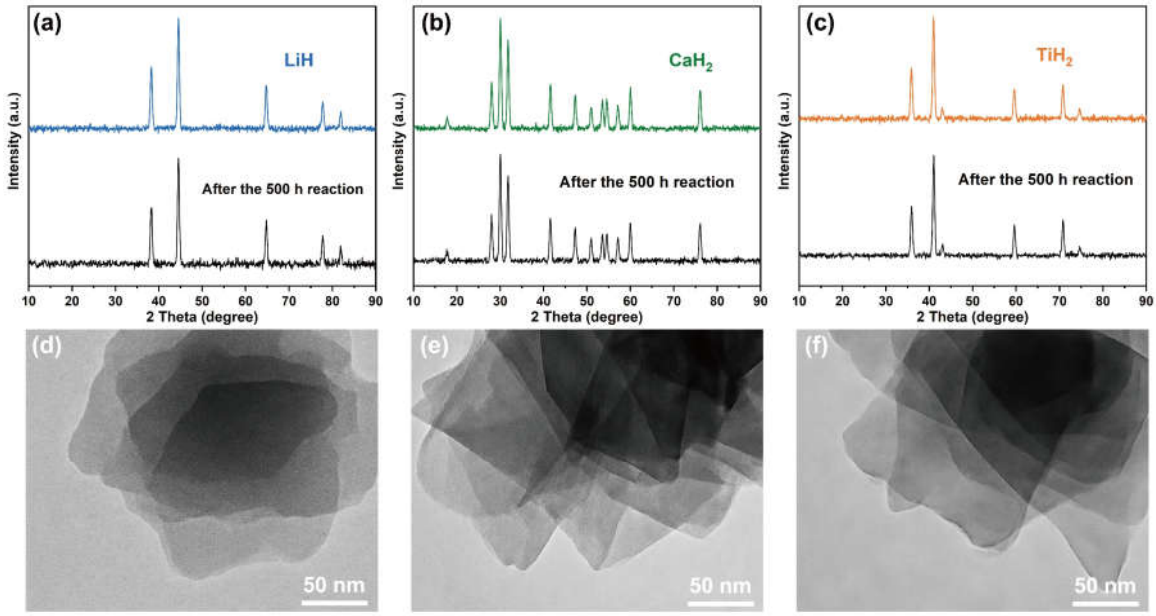

Figure S8 The XRD patterns of LiH (a), CaH_2 (b), and TiH_2 (c) catalysts before and after 500 hours of plasma–catalytic NH_3 synthesis tests. The SEM images of LiH (d), CaH_2 (e), and TiH_2 (f) catalysts after 500 hours of plasma–catalytic NH_3 synthesis tests.

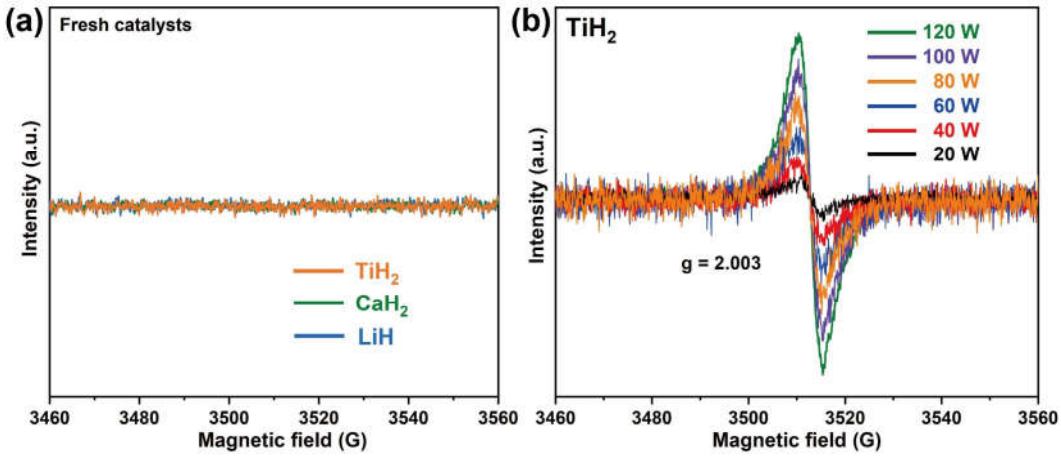

Figure S9 (a) The EPR results of fresh LiH, CaH_2, and TiH_2 catalysts before plasma–catalytic NH_3 synthesis tests. (b) The EPR results of TiH_2 under various input power levels.

Table S6 Position lifetime parameters of LiH, CaH_2, and TiH_2 after 500 hours tests.

Catalyst	τ_1 (ps)	τ_2 (ps)	τ_3 (ps)	I_1 (%)	I_2 (%)	I_3 (%)
TiH_2	226.2	496.7	3.2	29.6	68.3	2.1
CaH_2	209.3	450.4	3.04	46.8	51.8	1.4
LiH	164.2	423.6	2.64	63.6	35.6	0.8

6. Kinetic analysis

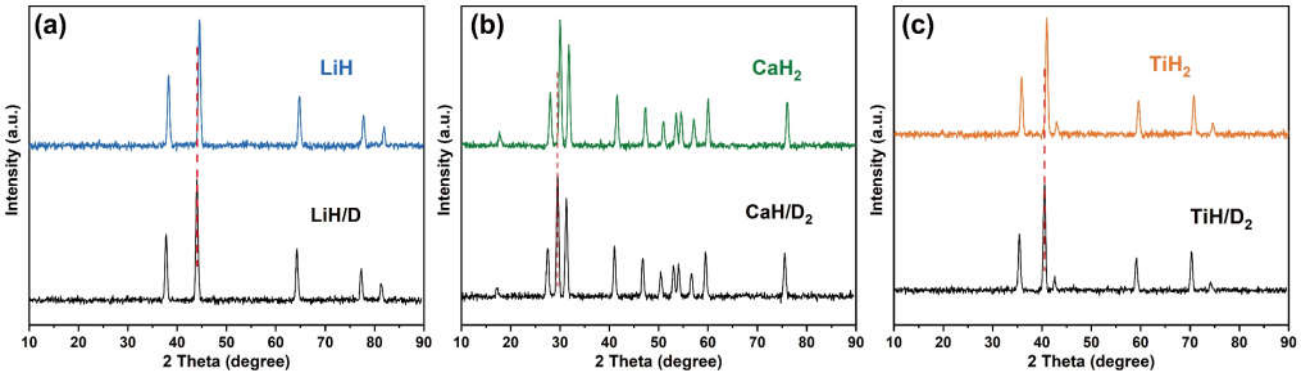

Figure S10 The XRD spectrum of LiH, CaH_2, and TiH_2 catalysts before and after the isotope tracking experiments.

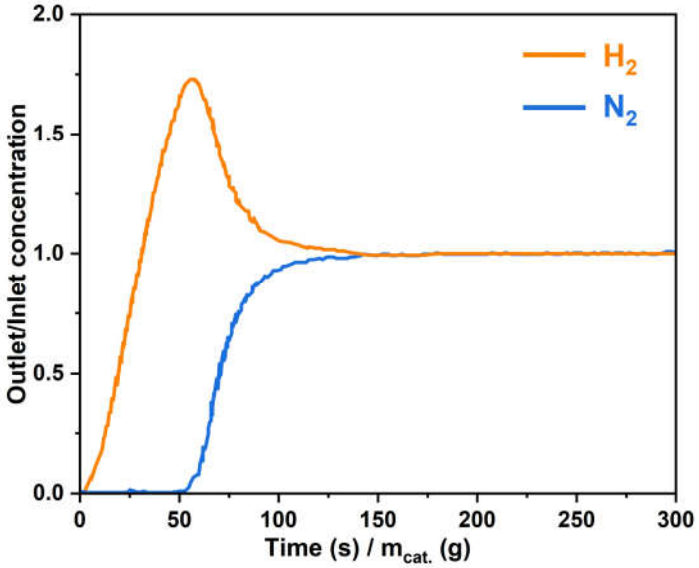

Figure S11 Breakthrough curves of the TiH_2 catalyst under N_2/H_2 (v/v, 2:3) mixture conditions at 298 K and 101 kPa.

7. Supplemental references

[1] P. Barboun, P. Mehta, F. A. Herrera, D. B. Go, W. F. Schneider and J. C. Hicks, *ACS Sustain. Chem. Eng.*, **2019**, 7, 8621–8630.

[2] D. W. Flaherty and A. Bhan, *J. Catal.*, **2024**, 431, 115408.

[3] S. Luo, Y. Liu, L. Guo, Y. Song, Y. Yang, F. Chen, L. Wang, Y. Chen, S. Chen and Z. Wei, *J. Mater. Chem. A*, **2025**, 13, 30546–30553.

[4] S. Luo, Y. Liu, Y. Song, Y. Yang, F. Chen, S. Chen and Z. Wei, *Chem. Commun.*, **2024**, 60, 3295–3298.

[5] S. Luo, Y. Liu, Y. Song, Y. Yang, D. Long, L. Li, S. Chen and Z. Wei, *Chem. Commun.*, **2025**, 61, 16066–16069.

[6] Y. Wang, W. Yang, S. Xu, S. Zhao, G. Chen, A. Weidenkaff, C. Hardacre, X. Fan, J. Huang and X. Tu, *J. Am. Chem. Soc.*, **2022**, 144, 12020–12031.

[7] T. Mizushima, K. Matsumoto, H. Ohkita and N. Kakuta, Plasma Chem. Plasma Process., 2007, 27, 1–11.

[8] G. Akay and K. Zhang, *Ind. Eng. Chem. Res.*, **2017**, 56, 457–468.

[9] P. Mehta, P. Barboun, F. A. Herrera, J. Kim, P. Rumbach, D. B. Go, J. C. Hicks and W. F. Schneider, *Nat. Catal.*, **2018**, 1, 269–275.

[10] Q. Xie, S. Zhuge, X. Song, M. Lu, F. Yu, R. Ruan and Y. Nie, *J. Phys. D. Appl. Phys.*, **2020**, 53, 064002.

[11] J. R. Shah, F. Gorky, J. Lucero, M. A. Carreon and M. L. Carreon, *Ind. Eng. Chem. Res.*, **2020**, 59, 5167–5176.

[12] S. Li, T. van Raak and F. Gallucci, *J. Phys. D. Appl. Phys.*, **2020**, 53, 014008.

[13] F. Gorky, S. R. Guthrie, C. S. Smoljan, J. M. Crawford, M. A. Carreon and M. L. Carreon, *J. Phys. D. Appl. Phys.*, **2021**, 54, 264003.

[14] X. Hu, X. Zhu, X. Wu, Y. Cai and X. Tu, *Plasma Process. Polym.*, **2020**, 17, 1–9.

[15] B. H. R. Suryanto, D. Wang, L. M. Azofra, M. Harb, L. Cavallo, R. Jalili, D. R. G. Mitchell, M. Chatti and D. R. MacFarlane, *ACS Energy Lett.*, **2019**, 4, 430–435.

[16] M. M. Shi, D. Bao, B. R. Wulan, Y. H. Li, Y. F. Zhang, J. M. Yan and Q. Jiang, *Adv. Mater.*, **2017**, 29, 1606550.

[17] J. Kong, A. Lim, C. Yoon, J. H. Jang, H. C. Ham, J. Han, S. Nam, D. Kim, Y.–E. Sung, J. Choi and H. S. Park, *ACS Sustain. Chem. Eng.*, **2017**, 5, 10986–10995.

[18] L. Zhang, L. X. Ding, G. F. Chen, X. Yang and H. Wang, *Angew. Chemie Int. Ed.*, **2019**, 58, 2612–2616.

[19] D. Bao, Q. Zhang, F.–L. Meng, H.–X. Zhong, M.–M. Shi, Y. Zhang, J.–M. Yan, Q. Jiang and X.–B. Zhang, *Adv. Mater.*, **2017**, 29, 1604799.

[20] H. Jin, L. Li, X. Liu, C. Tang, W. Xu, S. Chen, L. Song, Y. Zheng and S.–Z. Qiao, *Adv. Mater.*, **2019**, 31, 1902709.

[21] J. Wang, L. Yu, L. Hu, G. Chen, H. Xin and X. Feng, *Nat. Commun.*, **2018**, 9: 1795.

[22] S.–J. Li, D. Bao, M.–M. Shi, B.–R. Wulan, J.–M. Yan and Q. Jiang, *Adv. Mater.*, **2017**, 29, 1700001.

[23] N. Lazouski, M. Chung, K. Williams, M. L. Gala and K. Manthiram, *Nat. Catal.*, **2020**, 3, 463–469.

[24] H. K. Lee, C. S. L. Koh, Y. H. Lee, C. Liu, I. Y. Phang, X. Han, C.–K. Tsung and X. Y. Ling, *Sci. Adv.*, **2025**, 4, eaar3208.

[25] F. Zhou, L. M. Azofra, M. Ali, M. Kar, A. N. Simonov, C. McDonnell–Worth, C. Sun, X. Zhang and D. R. MacFarlane, *Energy Environ. Sci.*, **2017**, 10, 2516–2520.

[26] S. Z. Andersen, V. Čolić, S. Yang, J. A. Schwalbe, A. C. Nielander, J. M. McEnaney, K. Enemark–Rasmussen, J. G. Baker, A. R. Singh, B. A. Rohr, M. J. Statt, S. J. Blair, S. Mezzavilla, J. Kibsgaard, P. C. K. Vesborg, M. Cargnello, S. F. Bent, T. F. Jaramillo, I. E. L. Stephens, J. K. Nørskov and I. Chorkendorff, *Nature*, **2019**, 570, 504–508.

[27] G.–F. Chen, X. Cao, S. Wu, X. Zeng, L.–X. Ding, M. Zhu and H. Wang, *J. Am. Chem. Soc.*, **2017**, 139, 9771–9774.

[28] W. Liu, M. Xia, C. Zhao, B. Chong, J. Chen, H. Li, H. Ou and G. Yang, *Nat. Commun.*, **2024**, 15, 3524.

[29] J. Zheng, H. Zhang, J. Lv, M. Zhang, J. Wan, N. Gerrits, A. Wu, B. Lan, W. Wang, S. Wang, X. Tu, A. Bogaerts and X. Li, *JACS Au*, **2023**, 3, 1328−1336.

[30] J. Sun, D. Alam, R. Daiyan, H. Masood, T. Zhang, R. Zhou, P. J. Cullen, E. C. Lovell, A. Jalili and R. Amal, *Energy Environ. Sci.*, **2021**, 14, 865–872.

[31] Q. Cao, W. Wen, W. Sun, Y. Zhou and X. Yu, *Small*, **2025**, 21, e08642.

[32] L. Hollevoet, E. Vervloessem, Y. Gorbanev, A. Nikiforov, N. De Geyter, A. Bogaerts and J. A. Martens, *ChemSusChem*, **2022**, 15, e202102526.